The Role of Oxygen Vacancy on the Carbon Dioxide Photoreduction Using Monoclinic and Tetragonal-phase Zirconium Oxide

Ayana Omata, Keisuke Hara, Tomoki Oyumi, Rento Ishii, Yasuo Izumi, Kaori Niki [†]

Department of Chemistry, Graduate School of Science, Chiba University, Chiba
[†] *Corresponding author:* niki@chiba-u.jp

Various catalysts are used in processes for the conversion CO_2. Photocatalysts with higher concentrations of surface oxygen vacancies have been reported to exhibit excellent CO_2 photoreduction activity. This study systematically investigates monoclinic $ZrO_2(001)$ and tetragonal $ZrO_2(101)$ surfaces using experimental and theoretical approaches. Results of photocatalytic CO_2 conversion experiments under ultraviolet visible light irradiation showed formation rates of ^{13}CO on the surfaces of

monoclinic phase-major $ZrO_2(001)$ and tetragonal-phase $ZrO_2(101)$ of 0.65 and 0.041 $\mu mol\,h^{-1}\,g_{cat}^{-1}$, respectively. Dissociation of CO_2 was observed at the oxygen vacancy sites on both surfaces. Results of our calculations indicate that the second lowest unoccupied molecular orbital (LUMO+1) of CO_2 adsorbed on the site of the oxygen vacancy is located within the conduction band of monoclinic $ZrO_2(001)$ and facilitates the photodissociation of CO_2. Furthermore, oxygen vacancy sites were re-formed by H_2O desorption through the addition of hydrogen to monoclinic $ZrO_2(001)$. On the contrary, the desorption of H_2O at the oxygen vacancy sites are less likely to occur in tetragonal $ZrO_2(101)$, and this reduces the amounts of CO_2-to-CO conversion products.

Keywords *Carbon dioxide adsorption; Photocatalysis; Redox reactions; Zirconium oxide*

I. INTRODUCTION

It is necessary to develop a new carbon-neutral cycle by using sustainable energy sources and cheap materials to mitigate anthropogenic climate change. A promising approach in this domain is the conversion of CO_2 using photocatalysts [1, 2]. Examples of this approach include the conversion of CO_2 into carbon monoxide, formic acid, and methane on catalytic surfaces (TiO_2 [1, 3], NiO-TiO_2 [4], Ag-ZrO_2 [5], Ni-ZrO_2 [6, 7], Ni-SiO_2 [8], and Cu_3SnS_4 [9]), as well as the production of methanol on several catalyst surfaces (TiO_2 [1, 2], Ag-TiO_2 [10], and Pt-ZnO [11]). Relevant research has reported the usefulness of oxygen vacancies on the surface of metal oxide catalysts for such conversion processes [12–19]. Zhang *et al.* conducted experiments on the dissociation of CO_2 on the surface of monoclinic (m-)$ZrO_2(111)$ [5], observed high activity, and ascribed it to the regeneration of oxygen vacancies due to the addition of hydrogen during the reactions to perpetuate the
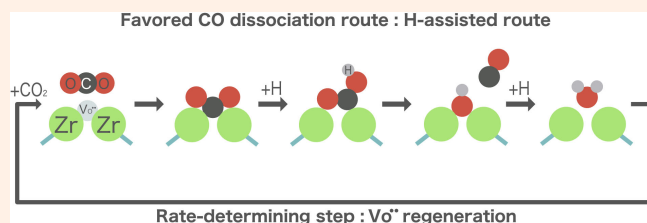
photoreaction cycle. Nevertheless, their work was limited to the (111) facet of monoclinic crystal, and few studies explored alternative facets or tetragonal crystals that inherently resist oxygen vacancies.

In this study, we use experiments and calculations to examine the dependence of the crystal structures of m-$ZrO_2(001)$ and tetragonal (t-)$ZrO_2(101)$ on their mechanisms for the photodissociation of CO_2. We first measure the magnitude of photocatalytic CO_2 conversion on their surfaces, and then assume various adsorption structures and determine the adsorption energy of each. The aim is to elucidate the pathway for the reaction on each surface.

Density functional theory (DFT) calculations were performed utilizing the Vienna *ab initio* simulation package (VASP), version 6.4.1 [20, 21]. Exchange correlation effects were described through the spin-polarized generalized gradient approximation (GGA) within the framework of the revised Perdew-Burke-Ernzerhof (RPBE) formalism [22]. A plane-wave basis set was employed in conjunction with the

projector augmented wave (PAW) method and an energy cutoff of 500 eV. Brillouin zone integration was conducted using a Monkhorst-Pack grid of $3 \times 3 \times 1$ k-points. To account for Fermi surface broadening, a Gaussian smearing of 0.05 eV was applied. Coulomb and exchange interactions of localized d-orbitals in transition metal elements were treated within the Dudarev DFT+U method, with the Hubbard U parameter of 4.0 eV set for Zr. The Hubbard U of 8.0 eV was recommended solely based on the bandgap agreement with experimental values. However, the Hubbard U below 4 eV was suggested when considering additional factors such as dielectric constant and other physical properties [23, 24]. The energy convergence criterion for self-consistency cycles was established at 1×10^{-6} eV. Optimization of ionic positions continues until the residual forces on each ion were reduced to below 1×10^{-1} eV Å^{-1}. These calculations encompassed long-range dispersion interaction (DFT-D3) as per Grimme's methodology, incorporating Becke-Jonson (BJ) damping [25–27]. In addition, transition states were calculated using the climbing image nudged elastic band (CI-NEB) method [28, 29].

We chose the surfaces of m-ZrO$_2$(001), containing ($2 \times 2 \times 2$) elemental unit cells, and t-ZrO$_2$(101), containing ($2 \times 1 \times 2$) and ($2 \times 1 \times 1$) elemental unit cells as slab models, with a vacuum spacing of 1 nm between the slabs [Figure 1(a–c)]. All surfaces were O-terminated. The green and red balls in these figures represent the zirconium and oxygen atoms, respectively.

The sites of surface oxygen vacancy sites [silver balls in Figure 1(a–c)] on ZrO$_2$ were modeled by removing the O atoms from the top layers of m-ZrO$_2$(001) and t-ZrO$_2$(101). (μ-Zr)$_2$ is an oxygen vacancy site (silver ball) that is in contact with two Zr atoms, as shown in Figure 1(a). (μ-Zr)$_3$ is an oxygen vacancy site (silver ball) that is in contact with three Zr atoms, as shown in Figure 1(b, c). The density of the vacancy sites is listed in Table 1. These values were calculated by assuming that there was one vacancy site per unit surface area of ZrO$_2$, as shown in Figure 1.

The formation energy (E_{vf}) of the oxygen vacancy sites was calculated based on Eq. (1);

$$E_{vf} = E(\text{Zr}_n\text{O}_{2n-1}) + E_{\text{O\_corrected}} - E(\text{Zr}_n\text{O}_{2n}), \quad (1)$$

where $E(\text{Zr}_n\text{O}_{2n-1})$ is the DFT energy of the slab containing an oxygen vacancy, $E_{\text{O\_corrected}}$ is half the value of the DFT energy of an isolated oxygen molecule with a correction (see SM 1 in Supplementary Material), and $E(\text{Zr}_n\text{O}_{2n})$ is the DFT energy of the slab.

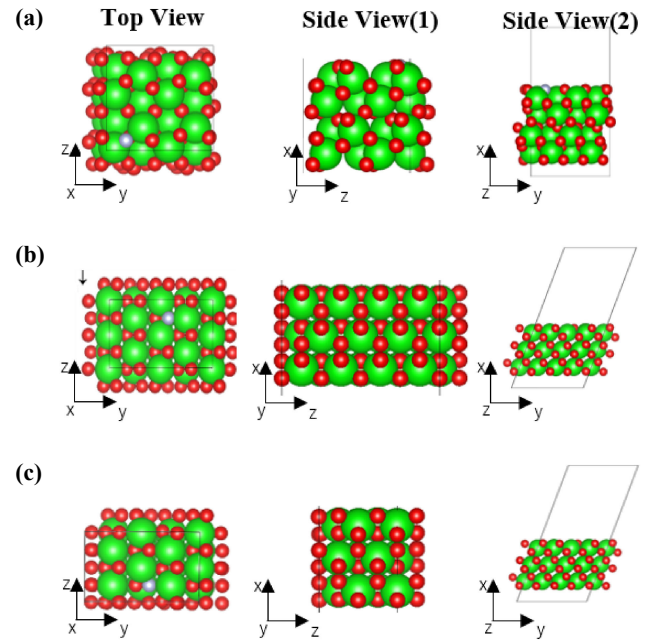The adsorption energy (E_{ads}) was calculated using the following equation;

Figure 1: (a) m-ZrO$_2$(001) faces with parameters of $x = 1.06$ nm, $y = 1.04$ nm, $z = 1.00$ nm, $\alpha = 90.00°$, $\beta = 90.00°$, and $\gamma = 90.00°$ with a 1.0-nm vacuum layer introduced in the direction of the z-axis. (b) t-ZrO$_2$(101) faces with parameters of $x = 1.45$ nm, $y = 1.27$ nm, $z = 1.63$ nm, $\alpha = 90.00°$, $\beta = 90.00°$, and $\gamma = 69.13°$ with a 1.0-nm vacuum layer introduced in the direction of the z-axis. (c) t-ZrO$_2$(101) faces with parameters of $x = 1.27$ nm, $y = 0.72$ nm, $z = 1.63$ nm, $\alpha = 90.00°$, $\beta = 90.00°$, and $\gamma = 69.13°$ with a 1.0-nm vacuum layer introduced in the direction of the z-axis. All lengths and angles are shown after structural optimization. Zr atoms, oxygen atoms, and oxygen defect positions are indicated by green, red, and silver balls, respectively.

$$E_{ads} = E_{mol/slab} - E_{mol} - E_{slab}, \quad (2)$$

where $E_{mol/slab}$, E_{mol}, and E_{slab} are the total energy of the slab with the adsorbate, the total energy of an isolated molecule in the gas phase, and the total energy of the slab, respectively.

II. EXPERIMENTS

Monoclinic phase-major ZrO$_2$ (JRC-ZRO-3, Catalysis Society of Japan; primary monoclinic and minor tetragonal phase; specific surface area, 94.4 m^2 g^{-1}), tetragonal-phase ZrO$_2$ (only tetragonal phase; specific surface area, 140.0 m^2 g^{-1}) twenty milligrams sample placed in a quartz U-tube connected to a Pyrex glass circulation system (206.1 mL) and treated in a vacuum (10^{-6} Pa) for 1 h. X-ray diffraction (XRD) was used to investigate the crystal system. H$_2$ gas

Table 1: Formation energy and population of oxygen vacancy ($V_O^{\bullet\bullet}$) sites.

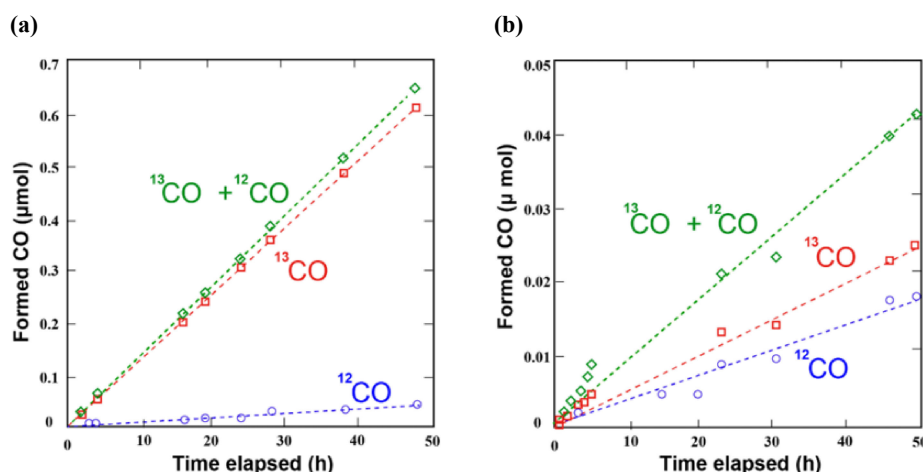| Surface	$E_{formation}$ (eV)	Population of $V_O^{\bullet\bullet}$ (nm^{-2})
(μ-Zr)$_2$ site on m-ZrO$_2$(001) comprising ($2 \times 2 \times 2$) element unit cells	6.51	0.8
(μ-Zr)$_3$ site on t-ZrO$_2$(101) comprising ($2 \times 1 \times 2$) element unit cells	6.57	0.5
(μ-Zr)$_3$ site on t-ZrO$_2$(101) comprising ($2 \times 1 \times 1$) element unit cells	6.66	1.1

(a)

(b)

Figure 2: Time course of photocatalytic tests using $^{13}CO_2$ (2.3 kPa) and H_2 (21.7 kPa) under UV-visible light irradiation over monoclinic-phase major (tetragonal minor) ZrO_2 (a) and tetragonal-phase ZrO_2 (b).

Table 2: Adsorption energy and adsorption-induced the O–C–O angle of CO_2 on the $V_O^{\bullet\bullet}$ site.

	Adsorption energy (eV)	O–C–O angle
m-ZrO_2(001) $2 \times 2 \times 2$	−2.6 [9]	132.06°
t-ZrO_2(101) $2 \times 1 \times 2$	−2.8	127.49°
t-ZrO_2(101) $2 \times 1 \times 1$	−2.7	127.49°

(20 kPa; purity > 99.99%) was introduced, and the temperature was increased to 723 K, maintained for 10 min, and treated in a vacuum. After that, $^{13}CO_2$ (2.3 kPa; ^{13}C 99.0%, purity > 99.9%, Cambridge Isotope Laboratories) and H_2 (21.7 kPa) were introduced into the system and irradiated by ultraviolet (UV)-visible light using a 500-W Xe arc lamp (SX-UID502XAM, Ushio) through a quartz fiber light guide (Model 1.2S15-1000F-1Q7-SP-RX, Optel) for 48 h. The reaction gas was monitored by online gas chromatography-mass spectrometry (GC-MS: JMS-Q1050GC, JEOL).

III. RESULTS AND DISCUSSIONS

A. Experimental results

As discussed, we tested the photocatalytic conversion of CO_2 by using two types of ZrO_2 photocatalysts (Figure 2). With $^{13}CO_2$, H_2, and monoclinic phase-major ZrO_2 under UV-visible light irradiation, the formation rate of ^{13}CO was 0.65 μmol h^{-1} g_{cat}^{-1}, and its ratio to the total CO content was 92 mol% differing from the 99% isotopic purity of the $^{13}CO_2$ reagent. This suggests a strong adsorption site for CO_2 on the ZrO_2 surface through the oxygen vacancies [5–7]. In contrast, the use of $^{13}CO_2$, H_2, and tetragonal-phase ZrO_2 with UV-visible light irradiation resulted in a ^{13}CO formation rate of only 0.041 μmol h^{-1} g_{cat}^{-1} [Figure 2(b)]. The ratio of ^{13}CO to that of total CO was 54 mol%. This lower ratio is attributed to reduced activity, with the contribution adsorbed $^{12}CO_2$ from air becoming more notable.

B. Calculation results
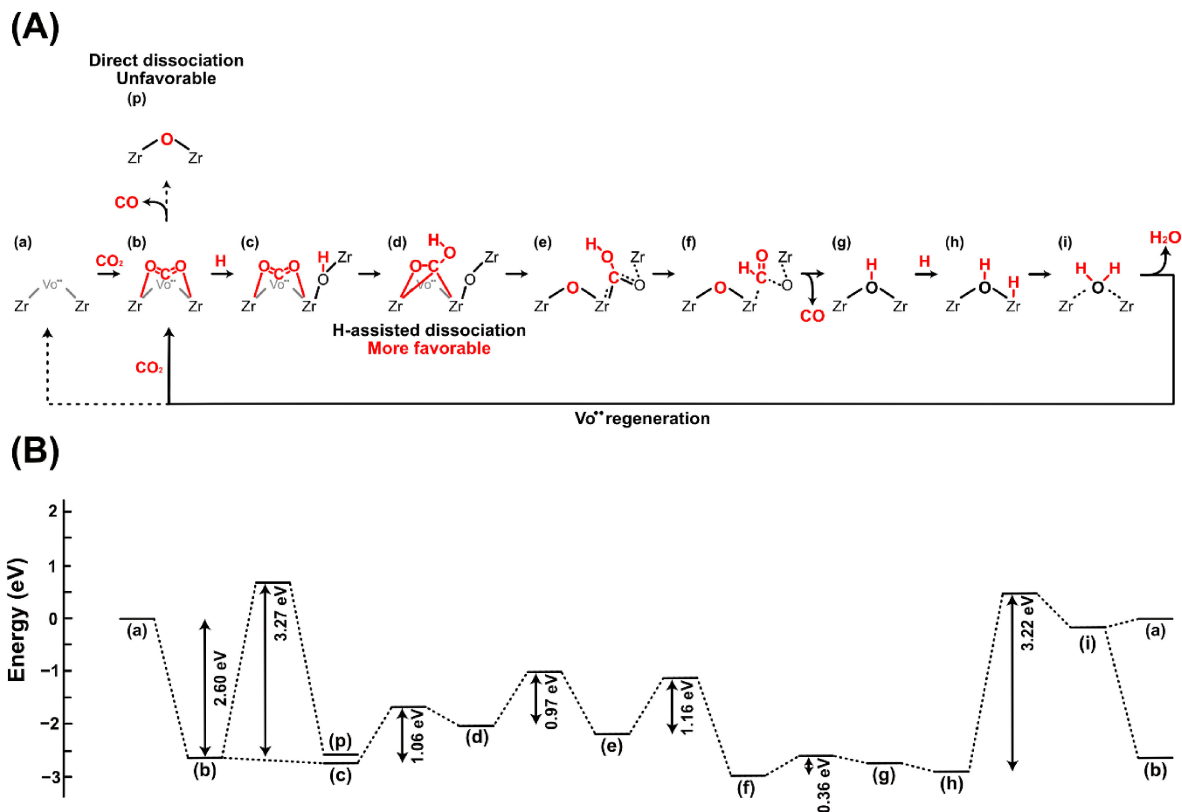
1. Reaction pathway of m-ZrO_2(001)

Based on the above calculations, we propose the pathway for the reaction shown in Scheme 1(A). We began with the structure containing only an oxygen vacancy on the surface, as shown in Scheme 1(A)(a). The processes of CO_2 adsorption [Scheme 1(A)(a, b)] and the initial dissociation of CO [Scheme 1(A)(b–g, b–p)] are followed by the regeneration of the oxygen vacancy [Scheme 1(A)(g–b)]. The addition of H atoms, which was also experimentally performed, led to the dissociation of CO [Scheme 1(A)(b–g)], followed by the desorption of H_2O to regenerate the oxygen vacancy [Scheme 1(A)(g–b)]. Specifically, the addition of the H atom [Scheme 1(A)(b, c)] enabled CO to dissociate while the remaining oxygen atom filled the vacancy [Scheme 1(A)(c–g)].

The reaction is driven by irradiated light (~5 eV), which covers all transition energies as shown in Scheme 1(B). Moreover, CO_2 in the adsorbed state has a lower energy level [Scheme 1(A)(b)] compared to H_2O in the adsorbed state [Scheme 1(A)(i)]. Consequently, H_2O desorbs from the vacancy of ZrO_2 while CO_2 undergoes adsorption. This facilitates the pathway for the dissociation reaction of CO_2 to form a cycle.

2. CO_2 adsorption on an oxygen vacancy

To explore the most favorable adsorption configuration, we examined the CO_2 adsorption states on ZrO_2 surfaces both with [Figure 3(a)] and without oxygen vacancy [Figure 3(c)]. Linearly arranged CO_2 molecules prior to adsorption were transformed into an M-shaped configuration upon adsorption, as is shown in Figure 3(b, d). The O–C–O angle was calculated to be 132.06° listed in Table 2.

The reduction of the adsorbed CO_2 occurred through structural change or an influx of charges from the substrate. Calculations of the Bader charge revealed that the carbon

Scheme 1: Proposed reaction pathways (A) and energetics (B) of CO_2 photoreduction energetically facilitated by the oxygen vacancy at the m-ZrO_2(001) surface.
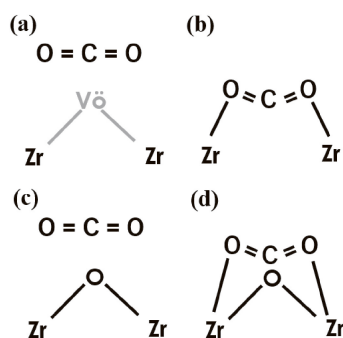

Figure 3: Schematic diagrams of the CO_2 adsorption process on m-ZrO_2(001). (a) An isolated CO_2 molecule and m-ZrO_2(001) surface with a $V_O^{\bullet\bullet}$ site, (b) CO_2 adsorbed on m-ZrO_2(001) with a $V_O^{\bullet\bullet}$ site, (c) an isolated CO_2 molecule and m-ZrO_2(001) surface without a $V_O^{\bullet\bullet}$ site, and (d) CO_2 adsorbed on m-ZrO_2(001) without a $V_O^{\bullet\bullet}$ site.

atom of CO_2 had a value of $+1.16$ [Figure 3(b)] upon adsorption, in contrast to the value of $+2.20$ for the carbon atom of the isolated CO_2 molecule. By filling the oxygen vacancy of ZrO_2 with the carbon atom of CO_2, the adsorption energy of CO_2 at the vacancy site was determined to be -2.60 eV. On the contrary, the adsorption energy on the vacancy-free surface was calculated to be -0.28 eV, indicating the stable adsorption of CO_2 on the vacancy site in ZrO_2.

The partial density of states (pDOS) provide a crucial insight into the electronic structure of adsorbed molecules and substrates, and the manner in which electron transitions occur when substances are excited by light. The calculation of the DOS on the surface of m-ZrO_2(001) without oxygen vacancies reveals a band gap of 3.94 eV, which closely aligns with the band gap obtained via DFT calculations by incorporating a Hubbard U parameter of 4 eV for the 4d orbitals of Zr [23]. By comparing the pDOS of the surface of m-ZrO_2(001) without [Figure 4(a)] and with [Figure 4(b)] oxygen vacancies, we observe that the formation of these vacancies leads to the development of a new state in the band gap. The valence band predominantly comprises O 2p orbitals, while the conduction band mainly consists of Zr 4d orbitals. The latter dominates the newly formed state, as shown in Figure 4(b), due to the presence of oxygen vacancies.

A state within the band gap, shown in Figure 4(c), is where CO_2 is adsorbed onto the oxygen vacancy in ZrO_2. Figure 5(a) shows the partial charge density associated with this state, corresponding to the lowest unoccupied molecular orbital (LUMO) of an isolated CO_2 molecule [Figure 5(b)]. Furthermore, Figure 5(c) depicts the partial charge density of the energy-minimized hybridized state in the conduction band of ZrO_2. This distribution resembles the LUMO+1 state of an isolated CO_2 molecule, as shown in Figure 5(d).

The LUMO state of the adsorbed CO_2 fell below the Fermi energy either through structural change or an influx of charges from the substrate. The LUMO+1 state was above the Fermi energy within the range of energy of the light source [200 nm (6.2 eV) to 800 nm (1.5 eV)]. The photoca-
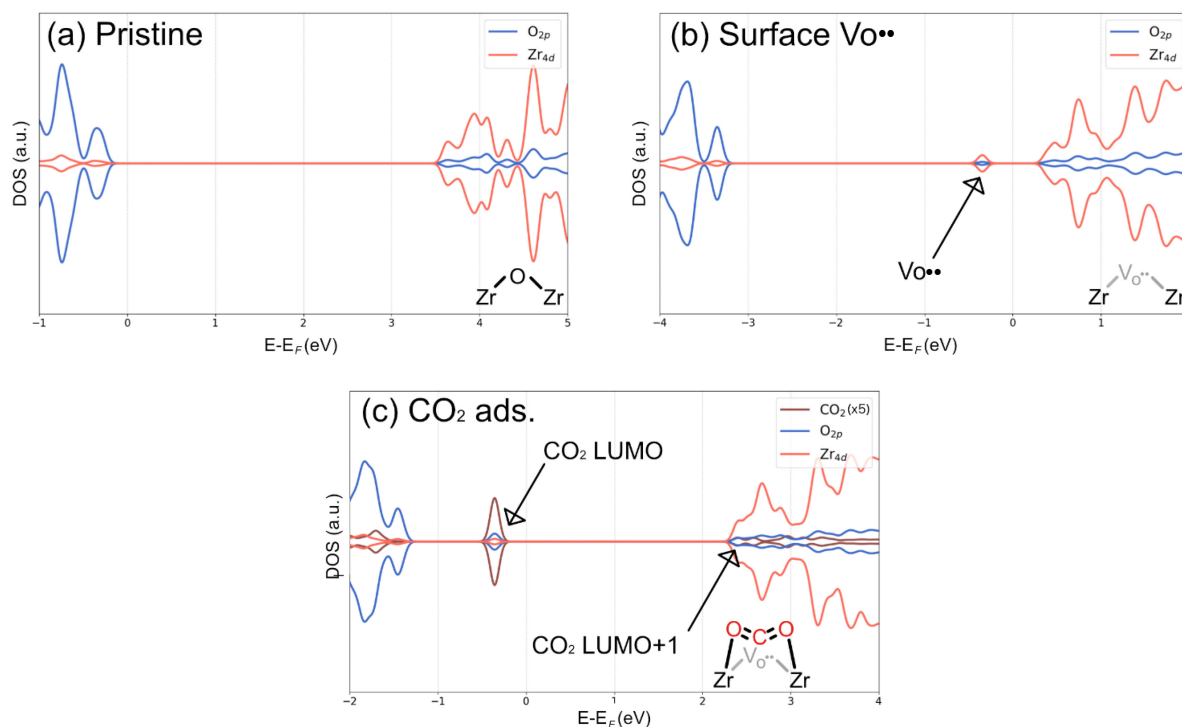
Figure 4: The pDOS on the m-ZrO_2(001) surface without $V_O^{\bullet\bullet}$ sites (a), with $V_O^{\bullet\bullet}$ sites (b), and the system with CO_2 adsorbed on the $V_O^{\bullet\bullet}$ sites (c). pDOS of CO_2 in Figure 4(c) is magnified by a factor of 5.
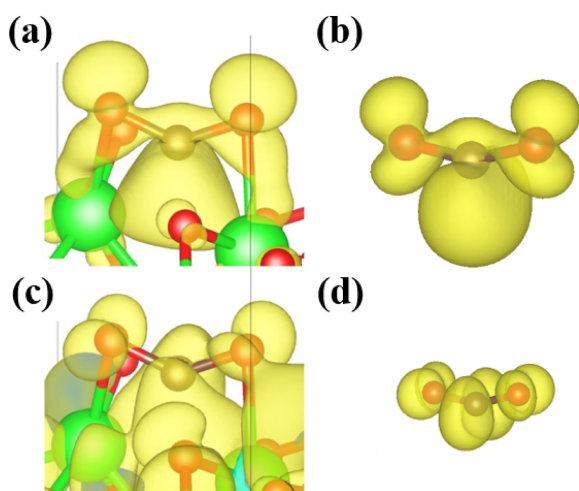

Figure 5: Visualization of partial charge density of an isolated state in the band gap (a) and LUMO of an isolated CO_2 (b), the state containing the CO_2 component closest to the conduction band minimum of ZrO_2 (c) and LUMO+1 of an isolated CO_2 (d).

talysis reaction in general progresses as excited electrons transfer from the substrate to the adsorbed molecules hybridized with conduction band of m-ZrO_2(001) through irradiation by light. We think that the LUMO+1 state of the adsorbed CO_2 is the most suitable destination for electrons of ZrO_2 that are excited by irradiation. The LUMO+1 state of the CO_2 adsorbed on the m-ZrO_2(111) surface did not hybridize with the conduction band of ZrO_2 [7], while strong hybridization was observed on the m-ZrO_2(001) surface.

This suggests that electrons of the valence band of the m-ZrO_2(001) surface could be directly injected into the LUMO+1 state of the adsorbed CO_2. This surface may yield a more efficient photocatalytic reduction of CO_2.

3. Vacancies regarding CO_2 dissociation

As mentioned above, CO_2 undergoes reduction through adsorption, and this might have facilitated the dissociation of CO [Scheme 1(A)(b–p)]. In this case, one oxygen vacancy of ZrO_2 remained occupied by an oxygen atom from CO_2. However, the high activity related to CO_2 reduction on the m-ZrO_2 surface has been explained above based on the regeneration of the oxygen vacancy [7]. The dissociation of the adsorbed CO_2 to LUMO+1 was promoted via a photo-excitation process that was characterized by nodes with a partial charge density, as shown in Figure 5(c), concurrently with the addition of hydrogen under excitation by photo-irradiation [Scheme 1(A)(b–g)]. The addition of the hydrogen atom subsequently led to the oxygen vacancy of ZrO_2 being filled with H_2O beyond the highest transition energy of 3.22 eV [Scheme 1(B)(h–i)]. When a water molecule was desorbed, an oxygen vacancy persisted. CO_2 was adsorbed into this vacancy, and this stabilized the ZrO_2 surface [Scheme 1(A)(i–b)].

4. Comparison of m-ZrO_2 and t-ZrO_2

The experimental results [Figure 2(a, b)] show the ratio of the volume of CO_2 to CO products as a function of time for monoclinic phase-major ZrO_2 and tetragonal-phase ZrO_2. $^{12}CO_2$ was the adsorbate initially present on the surface, of these compounds, whereas $^{13}CO_2$ was its isotope. Both were
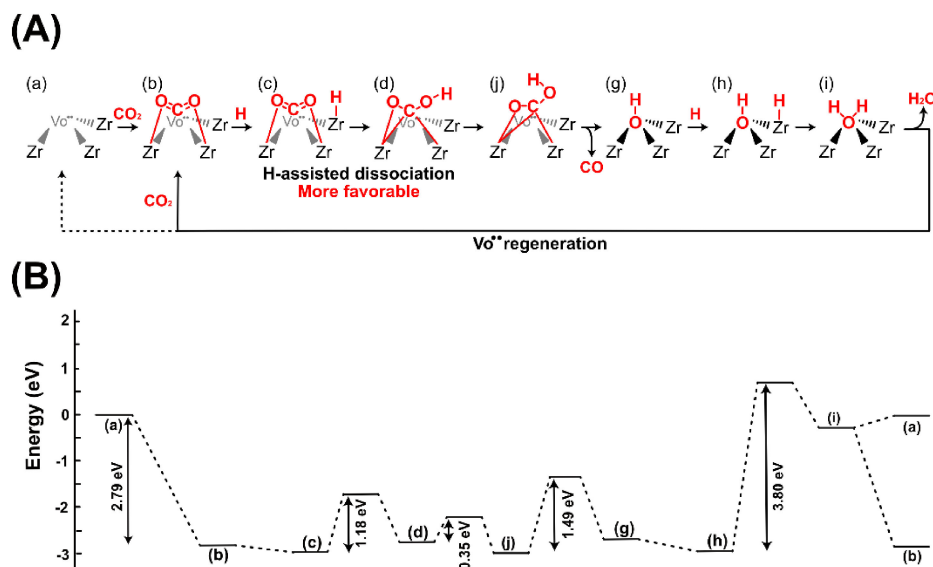
Scheme 2: Proposed reaction pathway (A) and energetics (B) of CO_2 photoreduction energetically facilitated by the oxygen vacancy at the t-ZrO_2(101) surface.
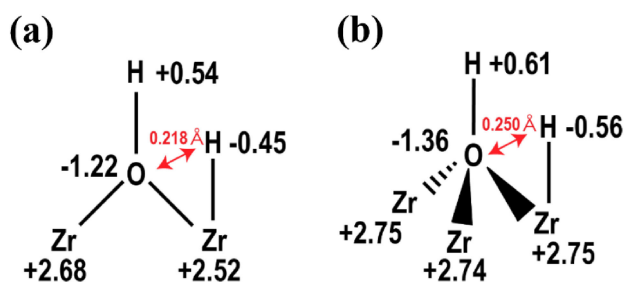

Figure 6: Bader charge and distance between atoms in Schemes 1(A)(h) and 2(A)(h): (a) m-ZrO_2(001) and (b) t-ZrO_2(101).

expected to dissociate CO_2 according to the processes detailed in Schemes 1 and 2. Comparison of the Figure 2(a, b) shows that the amounts of products on the surface of tetragonal-phase ZrO_2 was only about 1/10 of that on the surface of monoclinic phase-major ZrO_2. Furthermore, the number of products in the tetragonal phase decreases with time. We expected the vacancies to continue to be regenerated by H_2O desorption over time on m-ZrO_2(001), whereas we determined that H_2O desorption was less likely to occur on t-ZrO_2(101). The distance between the adsorbed oxygen atom and the hydrogen atom adsorbed on the adjacent Zr on t-ZrO_2(101) was larger than that on m-ZrO_2(001), suggesting that the desorption of H_2O was more difficult, as shown in Figure 6(a, b). This appears to be a difference in transition energies (0.58 eV) for H_2O configurations, as shown in Schemes 1(B)(h, i) and 2(B)(h, i).

IV. CONCLUSIONS

In this study, we performed experiments on m-ZrO_2(001) and t-ZrO_2(101) to analyze the photocatalytic conversion of CO_2 under UV-visible light irradiation, with the aim of elucidating the dependence of the surfaces and crystal structures of these compounds on the mechanism of CO_2 photodissociation. The formation rates of ^{13}CO on m-ZrO_2(001) and t-ZrO_2(101) were 0.65 and 0.041 µmol h^{-1} g$_{cat}$$^{-1}$, respectively. The formation rate of ^{13}CO on the surface of m-ZrO_2(001) is comparable to that on the surface of m-ZrO_2(111), whereas its formation rate on t-ZrO_2(101) is about 1/10 times lower. Furthermore, we considered various adsorption structures, corresponding adsorption energies, and the states of transition for the reaction. The states of transition were calculated using the CI-NEB method.

We used the above values to propose pathways for the CO_2 dissociation reaction on the surfaces of m-ZrO_2(001) and t-ZrO_2(101). CO_2 adsorbed on the oxygen vacancies of ZrO_2 on both surfaces underwent reduction through structural change or an influx of charges from the substrate.

With regard to the DOS of CO_2 adsorbed on oxygen vacancies on the surface of m-ZrO_2(001), the LUMO and LUMO+1 states of CO_2 were below the Fermi level and within the conduction band of m-ZrO_2(001), respectively. This suggests that electrons in the valence band of m-ZrO_2(001) should be photoexcited to the LUMO+1 state of CO_2 via electronic excitation to the conduction band of m-ZrO_2(001). This process is thought to facilitate dissociation of CO_2. The photoexcitation process should be more active in m-ZrO_2(001) than m-ZrO_2(111) [7], since the LUMO+1 state of CO_2 on m-ZrO_2(111) was observed to be beside the conduction band.

The oxygen vacancy on the surface of m-ZrO_2(001) was filled by a single oxygen atom that remained after the dissociation of CO_2 to CO. The oxygen atom that filled the vacancy was converted into H_2O by combining with experimentally added hydrogen atoms. Upon the desorption of H_2O, ZrO_2 reverted to the state of CO_2 adsorption, which was more stable than the state with the oxygen vacancy.

The distance between the O atom, which filled a vacancy on the ZrO_2 surface, and the hydrogen atom was larger in t-ZrO_2(101) than in m-ZrO_2(001). Therefore, vacancies were not easily regenerated in t-ZrO_2(101) and led to reduced activity on its surface. The added CO_2 was expected to continue filling vacancies on the surface of t-ZrO_2(101), thus reducing the volume of CO_2 dissociation at these sites. This explains why the rate of CO_2 dissociation decreased over time in our experiment on tetragonal-phase ZrO_2.

Acknowledgments

Appendix

The method for calculating $E_{O\_corrected}$ is found in Supplementary Material at https://doi.org/10.1380/ejssnt.2024-032.

References

[1] Y. Izumi, Coord. Chem. Rev. 257, 171 (2013).
[2] Y. Izumi, ACS Symposium Series 1194, 1 (2015).
[3] Y. Ji and Y. Luo, J. Am. Chem. Soc. 138, 15896 (2016).
[4] W. K. Fan, M. Tahir, H. Alias, and A. R. Mohamed, Int. J. Hydrog. Energy 51, 462 (2024).
[5] H. Zhang, T. Itoi, T. Konishi, and Y. Izumi, J. Am. Chem. Soc. 141, 6292 (2019).
[6] H. Zhang, T. Itoi, T. Konishi, and Y. Izumi, Angew. Chem. Int. Ed. 133, 9127 (2021).
[7] K. Hara, M. Nozaki, R. Hirayama, R. Ishii, K. Niki, and Y. Izumi, J. Phys. Chem. C 127, 1776 (2023).
[8] W. Wang and J. Gong, Front. Chem. Sci. Eng. 5, 2 (2011).
[9] N. Sharma, T. Das, S. Kumar, R. Bhosale, M. Kabir, and S. Ogale, ACS Appl. Energy Mater. 2, 5677 (2019).
[10] B. Yu, Y. Zhou, P. Li, W. Tu, P. Li, L. Tang, J. Ye, and Z. Zou, Nanoscale 8, 11870 (2016).
[11] S. M. Albukhari and A. A. Ismail, ACS Omega 6, 23378 (2021).
[12] Z. Su, W. Yang, C. Wang, S. Xiong, X. Cao, Y. Peng, W. Si, Y. Weng, M. Xue, and J. Li, Environ. Sci. Technol. 54, 12684 (2020).
[13] H.-F. Wang, H.-Y. Li, X.-Q. Gong, Y.-L. Guo, G.-Z. Lu, and P. Hu, Phys. Chem. Chem. Phys. 14, 16521 (2012).
[14] M. Wang, M. Shen, X. Jin, J. Tian, Y. Zhou, Y. Shao, L. Zhang, Y. Li, and J. Shi, Nanoscale 12, 12374 (2020).
[15] I. Hussain, G. Tanimu, S. Ahmed, C. U. Aniz, H. Alasiri, and K. Alhooshani, Int. J. Hydrog. Energy 48, 24663 (2023).
[16] Q. Liu, F. Wang, H. Lin, Y. Xie, N. Tong, J. Lin, X. Zhang, Z. Zhang, and X. Wang, Catal. Sci. Technol. 8, 4399 (2018).
[17] K. Kato, Y. Uemura, K. Asakura, and A. Yamakata, J. Phys. Chem. C 126, 9257 (2022).
[18] W. Wang and J. Gong, Front. Chem. Sci. Eng. 5, 2 (2011).
[19] S. A. Tolba and N. K. Allam, Sci. Rep. 9, 10159 (2019).
[20] G. Kresse and J. Hafner, Phys. Rev. B 47, 558(R) (1993).
[21] G. Kresse and J. Furthmüller, Phys. Rev. B 54, 11169 (1996).
[22] B. Hammer, L. B. Hansen, and J. K. Nørskov, Phys. Rev. B 59, 7413 (1999).
[23] M. Delarmelina, M. G. Quesne, and C. R. A. Catlow, Phys. Chem. Chem. Phys. 22, 6660 (2020).
[24] E.-S. R. Khattab, S. S. Abd El Rehim, W. M. I. Hassan, and T. S. El-Shazly, ACS Omega 6, 30061 (2021).
[25] S. Grimme, S. Ehrlich, and L. Goerigk, J. Comput. Chem. 32, 1456 (2011).
[26] S. Grimme, J. Antony, S. Ehrlich, and H. Krieg, J. Chem. Phys. 132, 154104 (2010).
[27] J. Moellmann and S. Grimme, J. Phys. Chem. C 118, 7615 (2014).
[28] G. Mills, H. Jónsson, and G. K. Schenter, Surf. Sci. 324, 305 (1995).
[29] G. Henkelman, B. P. Uberuaga, and H. Jónsson, J. Chem. Phys. 113, 9901 (2000).